



ENGINEERING

Ambient health sensing on passive surfaces using metamaterials

Dat T. Nguyen^{1,2,3†}, Qihang Zeng^{2,3†}, Xi Tian^{2,3,4†}, Patrick Chia⁴, Changsheng Wu^{3,4,5,6}, Yuxin Liu^{3,4,7}, John S. Ho^{1,2,3,4,5*}

Ambient sensors can continuously and unobtrusively monitor a person's health and well-being in everyday settings. Among various sensing modalities, wireless radio-frequency sensors offer exceptional sensitivity, immunity to lighting conditions, and privacy advantages. However, existing wireless sensors are susceptible to environmental interference and unable to capture detailed information from multiple body sites. Here, we present a technique to transform passive surfaces in the environment into highly sensitive and localized health sensors using metamaterials. Leveraging textiles' ubiquity, we engineer metamaterial textiles that mediate near-field interactions between wireless signals and the body for contactless and interference-free sensing. We demonstrate that passive surfaces functionalized by these metamaterials can provide hours-long cardiopulmonary monitoring with accuracy comparable to gold standards. We also show the potential of distributed sensors and machine learning for continuous blood pressure monitoring. Our approach enables passive environmental surfaces to be harnessed for ambient sensing and digital health applications.

INTRODUCTION

Advanced sensor technologies and machine learning have emerged as important tools for managing a wide spectrum of diseases, offering the possibility of continuous monitoring and personalized interventions (1, 2). While wearable devices have made remarkable progress in their comfort and sensing capabilities, their reliance on active user participation poses challenges in high-risk demographics, such as the elderly population. Ambient sensing offers an alternative approach that addresses these limitations by seamlessly capturing health data within physical spaces (3, 4). This approach allows for continuous and unobtrusive collection of health data, facilitating insight about health-critical activities in everyday environments (5).

Ambient sensing uses a variety of modalities for passive, non-contact health measurement, including wireless (6, 7), visual (8, 9), thermal (10, 11), and acoustics (12, 13) techniques. Among these, wireless sensors offer unique advantages due to their exceptional sensitivity to physiological motions, immunity to environmental lighting, and inherent privacy advantages (14–17). For example, wireless sensors have been used to remotely measure abdominal fat thickness (18), unobtrusively detect sleep apnea events (19), and perform continuous assessment of Parkinson's disease progression at home (20). However, wireless sensing of vital physiological parameters such as heartbeat and respiration remains challenging because everyday spaces contain many sources of background interference, in which the physiological signals of interest are masked by motions from other subjects and even other body regions

(Fig. 1A). In particular, a key limitation for existing wireless physiological sensing implementations is that they only provide single-channel cardiorespiratory signals, in contrast to the multichannel monitoring provided by clinical-grade sensors.

Textiles are ubiquitous in daily living environments, such as on clothing and furniture surfaces, because of their high mechanical conformability and durability to prolonged cyclic deformations. These properties make them a versatile platform on which to build sensors, particularly for ambient intelligence (21). Previous works have demonstrated advanced textile sensors that can detect mechanical stimuli, such as strain and pressure, using resistive, capacitive, triboelectric, or piezoelectric transduction mechanisms for vital sign measurement (22). Other works have also shown the feasibility of conductive textiles to be used as electrophysiological sensors (23). However, these sensors are contact-based and therefore have limited use in ambient sensing applications. While conductive textiles have been used to build radio-frequency devices such as antennas (24, 25), waveguides (26, 27), couplers (28), and resonators (29), these designs do not have capabilities in contactless health sensing.

Here, we present a technique to transform passive surfaces in the environment into contactless health sensors capable of detecting vital signs from multiple body regions. Our approach uses metamaterial textiles—structured conductive fabrics engineered to have unique electromagnetic properties (30). While prior research has reported using such metamaterials to enhance wireless networking for wearables (26) and implantable devices (31), our current work demonstrates their capability to mediate near-field interactions between body tissues and wireless signals for highly sensitive and interference-immune sensing of vital signs. The results are thin, conformal sensors that can integrate with everyday passive surfaces to offer accurate and reliable detection of subtle physiological motions from different body regions without requiring active user participation (tables S1 and S2). Using these sensors, we demonstrate continuous hours-long sensing of respiration rate (RR), heart rate (HR), and pulse rate (PR) with fidelity comparable to the gold standards (movie S1). We also show the potential of the technology for continuous cuffless blood pressure (BP) monitoring

¹Integrative Sciences and Engineering Program, National University of Singapore, Singapore 119077, Singapore. ²Department of Electrical and Computer Engineering, National University of Singapore, Singapore 117583, Singapore. ³Institute for Health Innovation and Technology, National University of Singapore, Singapore 117599, Singapore. ⁴SIA-NUS Digital Aviation Corporate Laboratory, National University of Singapore, Singapore 117602, Singapore. ⁵The N.1 Institute for Health, National University of Singapore, Singapore 117456, Singapore. ⁶Department of Materials Science and Engineering, National University of Singapore, Singapore 117575, Singapore. ⁷Department of Biomedical Engineering, National University of Singapore, Singapore 117583, Singapore.

*Corresponding author. Email: johnho@nus.edu.sg

†These authors contributed equally to this work.

using a machine learning model trained on data streams from two distributed sensors. Continuous ambient sensing experiments in an unstructured office space and a simulated airplane cabin demonstrate the versatility and robustness of the technology for contactless cardiopulmonary monitoring.

RESULTS

Metamaterial textile sensor

Figure 1B shows the ambient sensing concept in which passive surfaces in the environment are functionalized by metamaterial textiles to sense physiological motions using nonradiative wireless signals. These metamaterials consist of structured conductive fabrics supporting spoof surface plasmonic (SSP) modes (32), which extend from the textile surface without radiating into the surrounding space. Unlike prior research that focused on using such metamaterial textiles as passive conduits for wireless networking, we configure them to sense their surroundings using a software-defined radio (SDR) and optimize their design for physiological monitoring. Because of the evanescent nature of the modes, the resulting sensor is unaffected by external interference sources, such as wireless radiation in the

environment (fig. S1), background clutter (fig. S2), or movements of other individuals, and is highly sensitive to close-range interactions with body tissues (movie S2). Being thin and soft, the textile sensor can be easily integrated into everyday objects for the simultaneous monitoring of multiple localized vital signs on the body, such as heartbeat and radial pulse signals from the back and wrist (Fig. 1C). The SDR transmits a low-power continuous wave (CW) signal at $f_{RF} = 2.4$ GHz (Methods and fig. S3), which is guided conformally on the sensor surface at the shortened surface plasmon wavelength ($\lambda_{sp} \approx \lambda_0/2.85$) and couples into the body region. Larger Doppler phase variations compared to free-space radar signals can be obtained from the modulation of the wireless signal due to cardiopulmonary activity. The sensing region is sufficiently localized to detect physiological signals from body areas as small as the radial artery (fig. S4 and movie S3).

Figure 2A depicts the structure of the metamaterial textile, comprising a patterned conductive top layer, an intermediate nonconductive fabric layer, and a conductive bottom isolation layer. During each cardiac cycle, arterial perfusion leads to subtle permittivity changes (ϵ_r and ϵ_{blood}) due to variations in the local composition and boundary motion of tissues at the sensing sites. As the surface

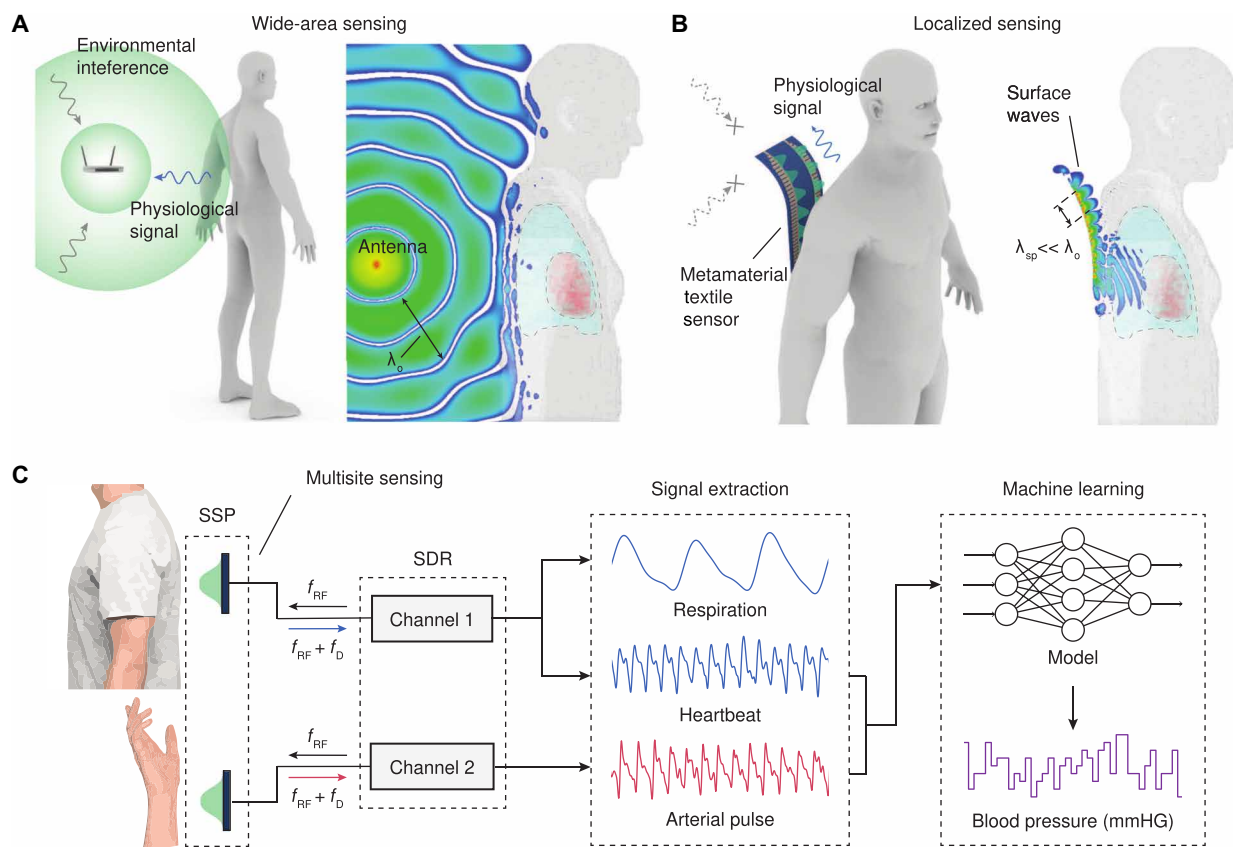


Fig. 1. Contactless near-field health sensing. (A) Conventional wireless sensing with radiative elements. Radiative sensing is inherently prone to many sources of environmental interference, such as from moving objects and people in the background, or movements of other body parts. λ_0 , free-space wavelength. (B) Contactless near-field health sensing based on metamaterial textile sensors. The immunity to distant interference sources is brought about by the nonradiating supporting spoof surface plasmonic (SSP) surface waves. The subwavelength energy confinement on the sensor leads to an enhanced coupling with tissues. The shortened surface plasmon wavelength ($\lambda_{sp} \approx \lambda_0/2.85$) results in amplified Doppler phase variations from cardiopulmonary-mediated impedance modulations. (C) Multisite tracking of physiological signals from different body parts enabled by the localized sensing property. Multichannel operation and advanced signal processing allow for the simultaneous extraction of multiple physiological targets.

waves evanescently couple to tissues, these signals manifest as Doppler phase variations resulting from cardiopulmonary-mediated impedance modulation of the metamaterial. Full-wave simulations of the metamaterial textile sensor demonstrate the confined surface waves' interactions with nearby computational arm and torso models, as shown in Fig. 2 (B and C). By using different fabric substrate materials and tuning the geometrical parameter h , the sensor can achieve SSP modes with varying degrees of wavelength confinement (fig. S5) and transmission loss (fig. S6), which govern the overall

sensitivity of the metamaterial sensor. To characterize the sensor's sensitivity in different configurations, we performed simulation studies using computational voxel models designed to mimic a cardiac cycle. For simplicity, we focus on investigating phase changes exclusively attributable to geometric variations of the radial artery and the heart during the cardiac cycle (Methods). This approach allows us to study the sensor's behaviors in the most conservative scenarios, where the surrounding multilayered tissues (table S3) are stationary and do not contribute to the sensor outputs. Figure 2

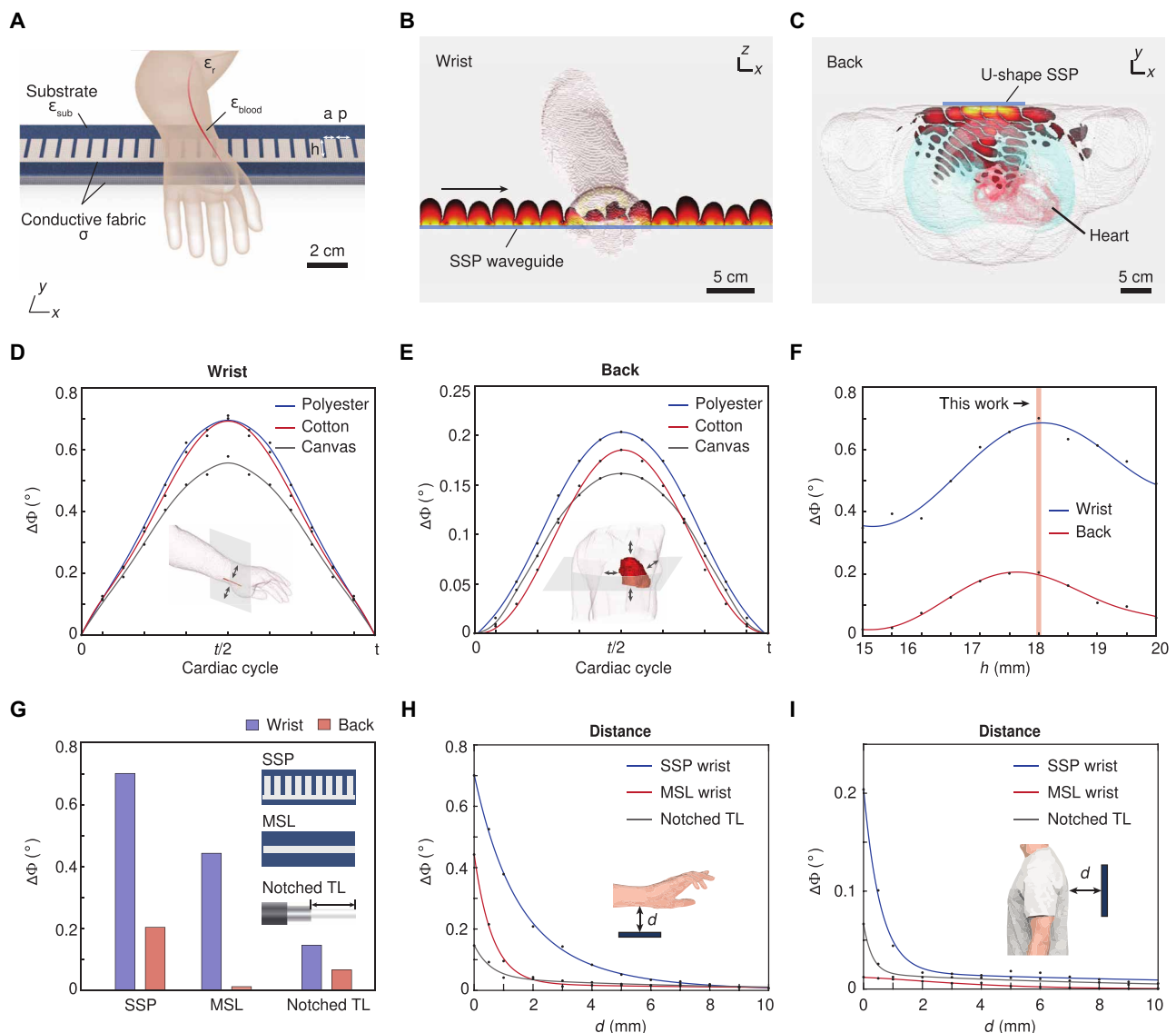


Fig. 2. Design and characterization of metamaterial textile sensor. (A) Illustration of an arm and its radial artery placed above the metamaterial textile structure with comb height h , comb width a , and pitch period p . σ , conductivity; ϵ_{sub} , substrate permittivity; ϵ_r , relative permittivity of tissue; ϵ_{blood} , relative permittivity of blood. Scale bar, 2 cm. (B and C) Full-wave simulations showing the cross sections of an arm (B) and a human body torso (C) during radial pulse and heartbeat sensing, respectively. Scale bars, 5 cm. (D and E) Simulated phase variations $\Delta\phi$ obtained from textile sensors with different fabric substrates due to a radial pulse (D) and a heartbeat (E) within a cardiac cycle. Insets show the respective arm and human torso simulation models. Arrows denote size variations of the radial artery and the heart in simulation. (F) Maximum simulated phase variations $\Delta\phi$ as obtained from textile sensors with different comb height h within a cardiac cycle. (G) Comparison of maximum simulated phase variations $\Delta\phi$ obtained from the supporting spoof surface plasmonic (SSP) sensor, an microstrip lines (MSL), and a notched transmission line (TL) within a cardiac cycle at the wrist and back. (H and I) Simulated phase variations $\Delta\phi$ against distance d from the wrist (H) and back (I) to the sensing surface of the metamaterial textile, the MSL, and the notched TL.

(D and E, respectively) shows the simulated phase changes within a cardiac cycle for different substrate materials. Because of the low relative permittivity of polyester ($\epsilon_r = 1.9$), a larger phase change can be obtained at both the wrist and the back compared to higher permittivity materials. To enhance sensitivity, a high degree of wavelength confinement (larger β) is desired, which can be achieved with larger h (fig. S7). However, since higher wavelength confinement increases transmission loss (fig. S6), Fig. 2F shows that increasing h beyond 18 mm results in high losses that diminish sensitivity, as seen from the decrease in the obtained phase change. Hence, we choose $h = 18$ cm in our design to maintain a transmission loss of less than 0.3 dB cm^{-1} when fabricated with conductive textile ($\sigma \approx 5 \times 10^3 \text{ Sm}^{-1}$) on polyester fabric substrates ($\epsilon = 1.9$). In addition, we design planar matching sections using gradient corrugated strip with linear taper to reduce the surface-to-propagation conversion loss from a 50-ohm port to 0.9 dB (fig. S8). Figure S9 shows the measured transmission coefficient S_{21} of the SSP sensor under different wrist pulse sensing distances, where the worst-case path loss is 23.4 dB when the skin contacts the sensing surface. At a 10-dBm transmit power, heartbeat signals can be obtained from the SDR output with a signal-to-noise ratio of 12.7 dB , as shown in fig. S10.

The high energy confinement and shortened wavelength of the propagating SSP modes substantially enhance the transduction of subtle tissue impedance modulations into large phase variations. In contrast, conventional waveguides, such as microstrip lines (MSLs), lack evanescent fields necessary for strong interaction with tissues (fig. S11), resulting in a lower coupling efficiency (fig. S12). Figure 2G shows a sensitivity comparison between our sensor, an MSL, as well as a notched transmission line (TL) structure that has been previously studied as respiration sensors (full cardiac cycle shown in fig. S13) (33). For radial pulse sensing, our sensor exhibits 1.6- and 4.8-times higher sensitivity than an MSL and a notched TL, respectively. Because of the deeper location of the heart in the body, phase variations due to heartbeat obtained from the back is lower than that from the wrist for all three sensors. Nevertheless, because of the higher coupling to tissue, phase changes obtained from our SSP sensor are respectively 16 and 3 times higher compared to that from the MSL and notched TL. As the separation distance d between the body and the sensing surface increases, the retrieved phase changes decrease because of weaker coupling (Fig. 2I). However, the metamaterial textile sensor consistently exhibits phase changes of at least 1.5 times larger than the other sensing structures for distances up to 3 mm, indicating a higher sensitivity to cardiopulmonary activities at the wrist and the back. In addition, the SSP modes can couple to the body through different clothing materials with minimal degradation to sensitivity (fig. S14).

Multisite physiological sensing

Our metamaterial sensor can be strategically placed at multiple locations on the surface of everyday objects for multisite sensing of vital signs. Figure S15 shows that the sensor is highly robust to folding and bending, maintaining transmission loss below 2 dB for bending radii as low as 1.25 mm in the x - y plane and 2 cm in the x - z plane. Hence, we used two sensor configurations, namely, a straight and a U-shape one, for conformal and versatile incorporation into tables and chairs (fig. S16). Figure 3A illustrates the sensor designs and placement strategy used to detect localized vital signs from different locations on the body. Specifically, channel 1 (CH1; U-shape)

provides RR and HR from the back, while channel 2 (CH2; straight) measures radial PR from the wrist (Methods).

Figure 3B shows an example of the detected breaths, heartbeats, and pulses on recorded signal segments overlaid with true beat labels obtained from their respective references, namely, respiratory belt, electrocardiogram (ECG), and finger photoplethysmography (PPG). Respiratory peaks measured by the sensor show close qualitative agreement with that obtained from the reference. In the heart and pulse signals, a consistent temporal shift between the detected and the reference beats is observed because of different choices of beat markers. Specifically, while the ECG R peaks and PPG peaks are conventionally used as beat locations, our algorithms detect the positive zero-intercepts as beats (Methods). We validate the sensing accuracy by performing three separate experiments with healthy human volunteers to benchmark the respiration, heart, and pulse beat-to-beat intervals (BBIs) against their references. The participants wore normal office attire and were instructed to minimize movements (Methods). The Bland-Altman analyses (34) in Fig. 3 (C to E) show biases of 0.594 , -0.143 , and 0.128 ms , respectively. The limits of agreement (LoAs) of approximately ± 0.28 , ± 0.08 , and $\pm 0.06 \text{ s}$, corresponding to ± 1.97 , ± 7.53 , and ± 5.45 beats per minute (BPM) for the three vital signs, respectively, are comparable to or better than previously reported accuracy of wrist-worn devices (35, 36).

Cuffless BP estimation

Continuous monitoring of BP is essential for managing hypertension and related cardiovascular diseases. Although cuff-based methods such as auscultation or oscillometry are the most widely used techniques, they are inconvenient, time-consuming, and noncontinuous. Our sensor's ability to contactlessly obtain accurate vital signs from multiple locations on the body facilitates cuffless BP sensing via pulse transit time (PTT) measurement (37). To do this, we developed a machine learning pipeline that automatically aligns our sensor outputs with the ECG R peaks and PPG maximum first derivative (MFD) points (38). Unlike conventional PTT measurements that rely on ECG and PPG sensors (39), our approach does not require mechanically stable skin contact, allowing for unobtrusive and continuous BP monitoring during daily living.

Figure 3E shows our "LSTM aligner" machine learning pipeline, which consists of two long short-term memory (LSTM) networks followed by fully connected (FC) layers working independently on each sensor channel. The aligned heart and radial pulse waveforms are obtained by minimizing the mean squared error (MSE) between the preprocessed phase signal inputs and target sequences (Methods and fig. S17). A 10-fold validation procedure shows under 40- and 80-ms average detection errors across all subjects, and evaluation on the testing dataset achieved average errors of 25.7 and 29.0 ms for the aligned pulse and heart signals, respectively (Methods and fig. S18). The Bland-Altman analysis of the calculated PTT from the LSTM aligner outputs versus reference ECG and PPG for 10 min of unseen data is summarized in Fig. 3G, showing a small mean bias of -0.192 ms and LoA within 50 ms .

Continuous health monitoring

The prevalence of sedentary lifestyles in the modern workplace (40) is associated with an elevated risk of cardiovascular diseases (41) and mortality (42). Long-term physiological monitoring in the office may therefore serve as an effective strategy to promote workplace health,

which can be realized by passively obtaining health metrics whenever the worker is in their work environment. To show our sensor's utility for this application, we performed an ambient vital sign sensing demonstration over a realistic 100-min working session with a healthy volunteer (Fig. 4A and Methods), whose movements in and out of the chair were not restricted. Figure 4C (i and ii) shows the raw

sensor data, which include artifacts due to motion, such as talking or typing on the computer. As motion artifacts result in false detection of heart and pulse beats, we defined a quality metric to prevent poor quality signals from degrading the overall accuracy in long-term monitoring (Methods and fig. S19). Robust vital sign detection was implemented by automatically detecting the “absent” periods, in

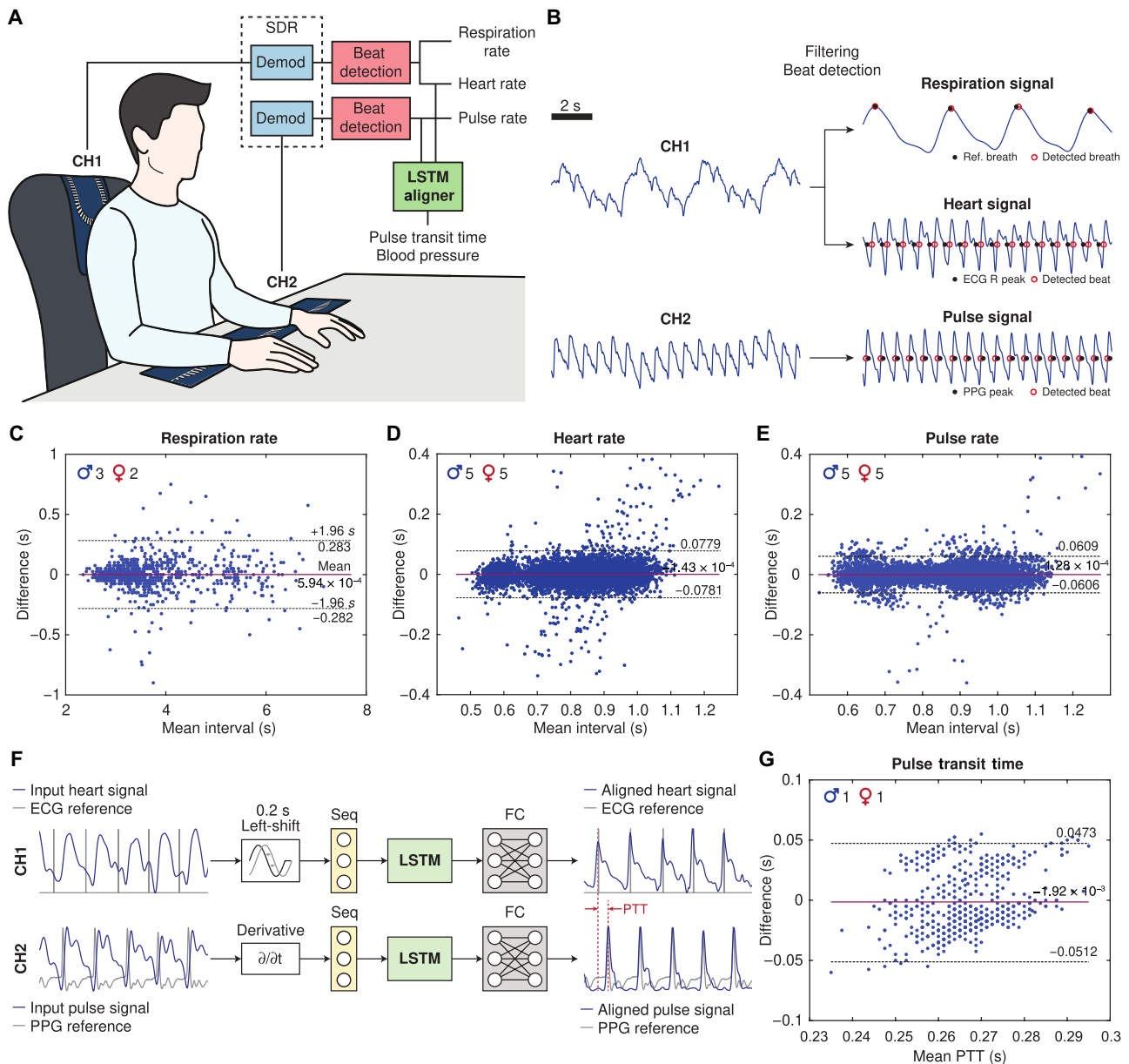


Fig. 3. Multisite physiological sensing evaluation. (A) Illustration of vital sign data collection setup. Vital signs from the back (respiration and heartbeat) and from the wrist (radial pulse) are respectively collected from channel 1 (CH1) and channel 2 (CH2) in the form of Doppler phase variations. Signals from CH1 and CH2 are demodulated in the software-defined radio (SDR) separately. Beat detection algorithms are developed for respiration, heartbeat, and pulse signals to extract the respective beat-to-beat rates. Heartbeat and pulse data collected are used by the long short-term memory (LSTM) aligner for PTT and blood pressure (BP) calculation. (B) Sample data collected from the two sensor channels. Beat-to-beat respiration rate (RR), heart rate (HR), and pulse rate (PR) can be obtained from filtering and beat detection algorithms. Scale bar, 2 s. (C to E) Bland-Altman plots of the BBIs obtained from our textile sensor and from reference measurements, showing the bias (mean, red solid lines) and LoA (black dotted lines) for (C) respiration, (D) heart, and (E) radial pulse. The data in each plot were collected in three separate experiments. The inset shows the respective number of male and female participants. (F) The LSTM aligner. The model performs heart (CH1) and pulse (CH2) signal alignment through two separate LSTM-based networks. Training was performed on all collected heart and pulse data. The LSTM aligner outputs heart and pulse signal waveforms with their peaks aligned to the reference ECG R peaks or PPG MFD points. Seq, sequence input layer; FC, fully connected layer. (G) Bland-Altman plot of the estimated PTT from testing data using LSTM aligner outputs and reference measurements. Testing data are dual-channel data collected from two subjects for 10 min each.

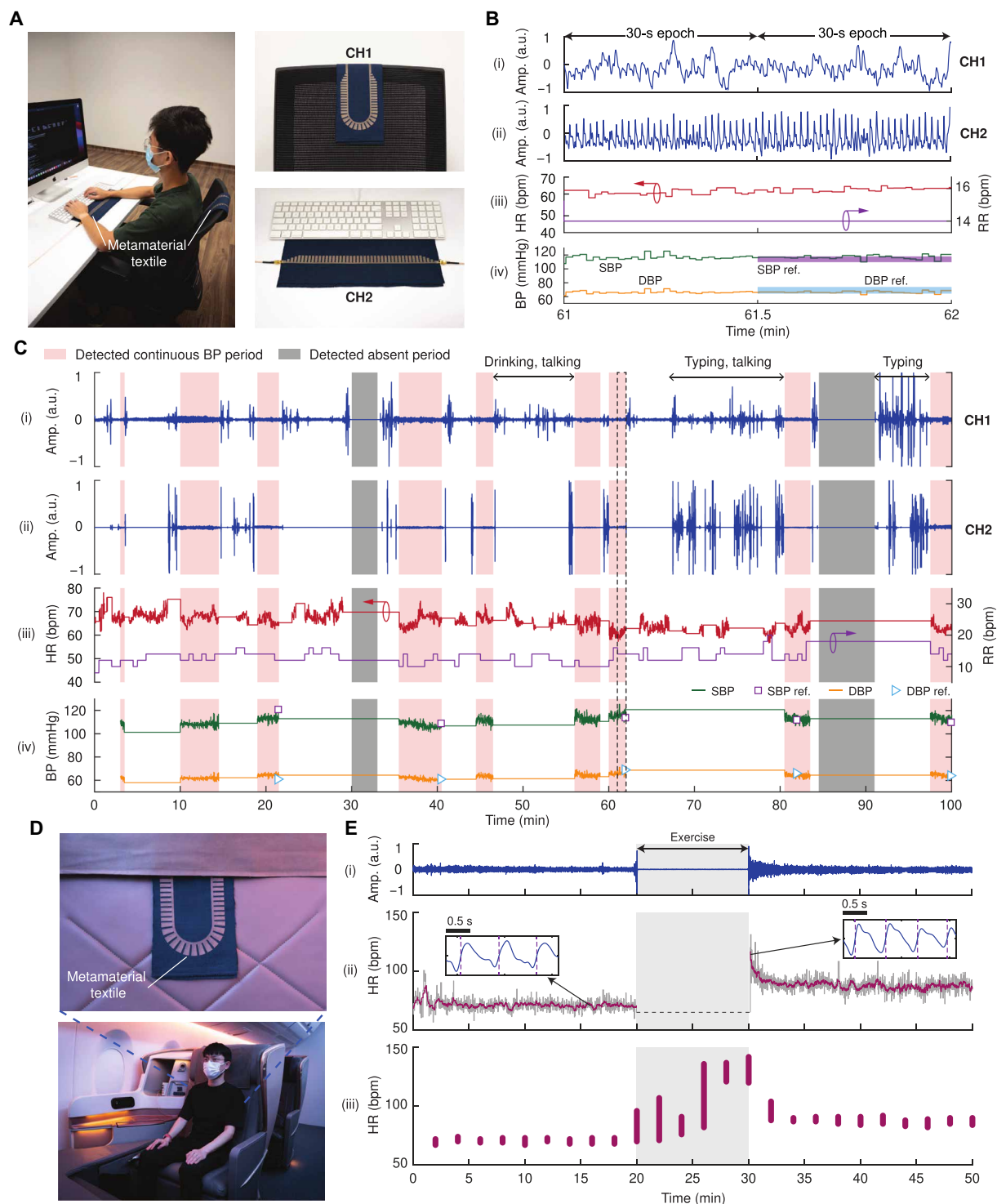


Fig. 4. Continuous ambient health monitoring. (A) Multisite health monitoring in an office environment using the dual-channel textile sensor system. Channel 1 (CH1) on the chair and channel 2 (CH2) on the desk recorded data simultaneously and continuously for 100 min. (B) (i and ii) Two 30-s epochs of normalized sensor outputs from both channels and (iii and iv) the detected vital signs including heart rate (HR), respiration rate (RR), systolic blood pressure (SBP), and diastolic blood pressure (DBP). Reference blood pressure (BP) measurements are shown for the second epoch. (C) Long-term health monitoring data throughout 100 min of working activities, showing (i and ii) the normalized sensor outputs and (iii and iv) detected vital signs. Automatically detected continuous BP and absent periods are labeled in pink and gray, respectively. Dashed lines represent the two epochs shown in (B). (D) Passenger health monitoring in an airplane cabin. (E) (i) Normalized sensor output. (ii) Detected continuous HR. Red line represents the moving average HR. Inset, enlarged plot showing sensor output waveform. Scale bars, 0.5 s. (iii) Reference HR measured with an Apple Watch, represented as bars showing the minimum-maximum range for every 2-min period. a.u., arbitrary units.

which the subject is not seated, as well as “continuous BP” periods, where high-quality data are available from both sensor channels for BP calculation (Methods and fig. S20). Although periods of noninteraction result in gaps in the sensor outputs, continuous HR and respiration can be obtained without active participation at all times that the subject is present in the intended sensing environment, as shown in Fig. 4C (iii). Figure 4C (iv) shows the systolic BP (SBP) and diastolic BP (DBP) estimated from the PTT values during each continuous BP epoch (fig. S21). Enlarged plots of two representative epochs at the 61-min mark of the experiment show continuous waveforms corresponding to the BP over each cardiac cycle (Fig. 4B). This capability in continuous BP waveform measurement stands in contrast to conventional cuffed BP measurements that provide a single averaged estimate over each trial.

The versatility of our textile sensor system extends its application into many other environments. Using an aircraft cabin simulator, we demonstrate our sensor’s ability to realize an in-flight ambient monitoring application. Continuous health monitoring of pilots and aircrew members is instrumental to preventing fatigue-related aviation accidents (43) through early detection of physiological abnormalities. In addition, in-flight monitoring of passenger wellness can also serve as a tool to minimize in-flight medical emergencies. As shown in Fig. 4D, our textile sensor can be attached to the backrest of an airplane seat to function as a soft and unobtrusive in-flight health tracker. To evaluate the sensing capability, we performed a 50-min continuous HR monitoring trial with a healthy male volunteer (Methods). Figure 4E shows the normalized output from our sensor with the extracted HR, as well as the HR collected from an Apple Watch as a reference. We show our sensor’s ability to capture a wide range of HR by increasing the subject’s HR through 10 min of exercise. Our sensor detected a 74-BPM increase in beat-to-beat HR from 57 to 131 BPM, which then tapers off to an elevated resting HR of ~85 BPM after 15 min of rest. These results agree well with the reference, demonstrating the potential of our sensors for ambient contactless physiological monitoring in a wide range of complex environments.

DISCUSSION

We have demonstrated a wireless sensing technique based on metamaterials that enables the transformation of passive textile surfaces into ambient contactless physiological sensors using the close-range interaction between SSP surface waves and the human body. Leveraging recent advances in e-textiles, we designed thin and flexible textile sensors for integration with furniture surfaces to realize an unobtrusive ambient sensing system capable of multisite physiological sensing from the back and the wrist. Simulation studies with computational voxel models illustrated the sensors’ phase response to conservative changes in geometry of the radial artery and heart during the cardiac cycle. In practice, cardiac activities involve a combination of changes in the position and composition of surrounding tissues, including the skin, fat, and muscle, manifesting as large Doppler phase variations captured by an SDR. Through experiments with healthy volunteers, we show our sensing system’s ability to detect multiple vital signs continuously, including respiration, heart, and radial pulse BBIs with accuracy comparable to gold-standard measurements. In addition, we demonstrate our sensors’ ability to estimate continuous cuffless BP aided by machine learning. Last, we show our sensor’s versatile practicality for monitoring

of multiple physiological signals in an unstructured office space and a simulated airplane cabin.

The ability to ubiquitously monitor health and wellness in ambient spaces can revolutionize preventive and personalized health care. To realize this vision, future work could explore the integration of metamaterial textile sensors into a wider range of ambient environments and investigate their effectiveness for chronic disease diagnosis and management. For example, unobtrusive monitoring of vital signs during sleep can be explored through the integration of these sensors into bedding materials, such as mattresses, comforters, or bedspreads, potentially serving as an at-home diagnostic tool for sleep disorders. Although our system currently relies on bulky SDR instrumentation to operate (fig. S22), future work may develop miniaturized, application-specific radar integrated circuits (44) that can be integrated seamlessly with the metamaterial textile for ubiquitous applications in daily living spaces. Last, exploring sensing based on existing communication protocols such as Bluetooth Received Signal Strength Indicators (45) or WiFi Channel State Information (46) can open up new opportunities in adapting SSP sensors to current consumer electronics and encourage widespread adoption.

METHODS

Electromagnetic simulations

CST Microwave Studio (Dassault Systems) was used for electromagnetic simulations. Materials for substrate fabric were assigned with $\epsilon_{\text{cotton}} = 1.6$, $\epsilon_{\text{polyester}} = 1.9$, and $\epsilon_{\text{canvas}} = 2.1$ (47). Computational arm and body voxel models were used to simulate field distributions. The resolution of the voxel was $2 \text{ mm} \times 2 \text{ mm} \times 2 \text{ mm}$. Cardiac cycle simulations of the radial pulse and heartbeat were conducted by periodic geometrical variations on the voxel models of the radial artery and the heart. The simulated tissue motions lead to changes in effective permittivity, which are demodulated as phase variations $\Delta\phi$ of the scattering parameter S_{21} . Best-fit lines were generated using the MATLAB Curve Fitting Toolbox.

Sensor fabrication

To fabricate the metamaterial sensors, commercially available conductive textiles (Holland Shielding Systems) were patterned by laser cutting (Universal Laser Systems, VLS 2.30) and attached to polyester fabric sheets. SubMiniature version A (SMA) connectors were attached by adhesive coating using conductive epoxy (CW 2460, Chemtronics) at room temperature.

Hardware setup

The sensing system prototype was implemented by connecting the terminals of the sensors with an SDR (Ettus B210 USRP, National Instruments) with coaxial cables (fig. S22). A laptop computer is used to power and communicate with the SDR over USB. Controls of the SDR were performed using GNURadio. The SDR is programmed to transmit (Tx) and receive (Rx) CW signals at the carrier frequency $f_{\text{RF}} = 2.4 \text{ GHz}$, with the baseband tone set at $f_{\text{BB}} = 10 \text{ kHz}$ sampled at 1 MHz . At 10-dBm Tx power, the simulated whole-body averaged specific absorption rate is 0.019 W/kg , well below the IEEE C.95.1–2019 limit of 2 W/kg (48). The digital complex Doppler signals were obtained by conjugate multiplication of the baseband Tx signal and the Rx signal after downconversion. The time-varying Doppler phase is then

obtained by arctangent demodulation and unwrapping of the complex Doppler signal.

Physiological signal processing

The sensor outputs were processed in MATLAB (R2021a, The MathWorks Inc.) to obtain respiration, heart, and pulse BBIs. The signals were downsampled to 400 Hz before processing. The reference heart and pulse beat information were obtained directly from the BIOPAC Student Lab Software.

Respiratory cycle detection

We implemented a respiratory peak detection algorithm based on moving-average curve (MAC) intercepts (49) on both our sensor data and the BIOPAC reference data. The signals were first band-pass filtered between 0.1 and 0.8 Hz, and fast Fourier transform was applied on the first 15 s of each signal segment to estimate a respiratory period T_{est} . The MAC was calculated at every point by taking the mean of the sensor outputs over a time window equivalent to $2T_{\text{est}}$. The intercepts between the sensor signal and its own MAC are labeled as either up or down intercepts based on the slope of the signal at that point. Last, a peak is detected as the maximum between an up intercept and its ensuing down intercept, and a respiratory cycle is calculated as the time duration between two adjacent peaks.

Heart and pulse beat detection

To extract the heart or pulse beats, we implemented a zero-crossing detection algorithm with adaptive thresholds based on the Pan-Tompkins algorithm (50, 51). In the preprocessing steps, the heart or pulse waveforms were first obtained by band-pass filtering the sensor data from 0.9 to 5 Hz to remove DC drifts, respiration, and high-frequency noise. We calculated the first derivative waveform, half-wave rectified it (set all negative values to zero), and then squared the resultant waveform to minimize small noise peaks. The squared signal is passed through a moving-average filter with 150-ms windows to produce an integrated signal used in the subsequent beat detection. The peaks in the band-pass filtered signal are detected using adaptive thresholding and decision rules according to the original Pan-Tompkins algorithm, which are then used as fiducial markers for the heart or pulse beat locations. The final beat locations are calculated as the nearest preceding positive zero-intercept to each fiducial marker in the band-pass filtered signal. The BBIs are then obtained as the interval between successive beat locations. Figure S23 shows a diagram describing the signal processing pipeline.

Evaluation of physiological sensing accuracy

Evaluation of respiration, heart, and pulse sensing accuracy was performed in three separate experiments. For each experiment, we recruited healthy participants (20 to 35 years of age) with no known preexisting cardiopulmonary conditions (table S4) from the National University of Singapore campus through advertisements by posted notices. Participants wore normal office attire, such as T-shirts and blouses. All experiments were performed in an open dry-laboratory space, in the presence of other laboratory members unrelated to the experiments. Each trial includes the recording of 10 min of data per participant. Reference data were measured using the BIOPAC MP46 2-channel data acquisition unit connected to the relevant compatible respiration, ECG, or PPG transducers, powered by a laptop computer and controlled with the BIOPAC Student Lab Software.

Respiration and heartbeat sensing

To collect the respiration and heartbeat data, a single textile sensor was attached to the backrest of an office chair. The participants were instructed to sit upright on the chair and rest lightly on the backrest. The sensor was connected to CH1 of the SDR, and the Doppler signals were recorded using the laptop computer. The participants were asked to breathe normally while minimizing limb movements. For each of the respiration and heartbeat sensing evaluations, the reference signals were respectively collected using a respiratory effort transducer (SS5LB, BIOPAC Systems Inc.) fastened around the participant's thorax, or a three-lead ECG transducer (SS2LB, BIOPAC Systems Inc.) attached to the participant's legs and right arm. The synchronization of recorded physiological signals from our sensor measurement and the reference was performed using system time stamps obtained from screen video recordings.

Arterial pulse sensing

For arterial pulse data collection, a single textile sensor was placed on an office table and connected to CH2 of the SDR. The participants were instructed to place either their right or left wrist on the sensor, with the radial artery directly on top of the conductive textile, and asked to breathe normally while minimizing movements. The Doppler signals from the arterial pulse motions were recorded in the same manner as the respiration or heartbeat evaluation experiment. The reference pulse signals were collected simultaneously using a finger PPG sensor (SS4LA, BIOPAC Systems Inc.) fastened on the index finger on the same side as the wrist under measurement.

LSTM aligner and PTT calculation

Dataset preparation

Heart and radial pulse signals collected during accuracy evaluation experiments from all subjects were used as training data for the LSTM aligner. We constructed two separate datasets to train the respective networks for heartbeat and pulse alignment. We preprocessed the heart signals by performing a 0.2-s left shift and the radial pulse signals by taking their time derivative. The input features were constructed by first generating incrementally left-shifted copies of the preprocessed signals in steps of five samples until the desired number of features is obtained. The features were then split into 5000-sample nonoverlapping windows, corresponding to 12.5 s, producing training samples of size $N \times 5000$, where N is the number of features (fig. S17). The testing dataset was constructed using additional dual-channel data separately collected from two healthy volunteers for a total of 10 min. All data processing, network training, and evaluation were performed in MATLAB (R2021a, The MathWorks Inc.).

LSTM aligner training and validation

The LSTM aligner comprises two LSTM-based networks for heartbeat and pulse signal alignment, which differ in the number of input features (15 and 5, respectively). In each network, a Seq layer is used to feed the training samples into the LSTM layer (80 hidden units), followed by a 20% dropout and an FC layer. A regression layer is used to minimize the MSE loss between the FC layer output and the training target. The overall structure of the network is shown in fig. S17, and the network parameters are detailed in table S5. We evaluated the LSTM aligner's ability to generalize across unseen subjects through a subject-based cross-validation process. For every subject, each network is trained using the data from the other nine subjects and then evaluated on that subject, thus forming a 10-fold cross-validation procedure. Detection error is defined as the time

difference between a detected beat and its corresponding reference beat. Last, the respective networks are trained on all training data, followed by evaluation on the testing dataset (fig. S18).

PTT calculation

PTT calculation is performed on LSTM aligner's outputs, starting with peak detection on the aligned heart signal. For each located peak, the algorithm searches the corresponding aligned pulse signal for a local maximum within its ensuing 0.15 to 0.4 s. The algorithm also searches for and removes falsely detected peaks by detecting outliers in the BBIs [defined as values that are more than five scaled median absolute deviations (52) from the median of all BBIs in an epoch or recording], which are calculated as an intermediate step.

Continuous health monitoring experiment

Evaluation of the sensing system for continuous health monitoring was performed with one healthy male subject for 100 min using the dual channel system. The subject was instructed to sit on the chair and perform regular tasks on the computer such as reading, using the mouse, and typing on the keyboard as required during the normal course of work. Movements of the arms and legs and other activities such as drinking, talking with others, as well as getting up from sitting positions were not restricted. During this period, other workers in the same office were also free to move about. Data are collected continuously from both channels throughout the entire duration of the experiment. A digital sphygmomanometer (OMRON HEM-7156-A) was used to provide reference BP measurements from the left arm in approximately 20-min intervals, for a total of five measurements. At 2 min before each reference measurement, the subject was instructed to place his right wrist on CH2 for pulse sensing until the reference BP values have been successfully recorded. We preprocessed the sensor outputs by dividing them into nonoverlapping 30-s epochs, each containing two channels of data. Beat-to-beat HR and RR were calculated from CH1 outputs. Epochs with large movement present were excluded from the rate calculations. To calculate BP values from PTTs, we used a linear relationship between PTT and BP obtained from a separate calibration by least squares regression of measured PTT and BP pairs (fig. S21).

Signal quality metric

To improve robustness against motion artifacts, we defined a signal quality metric based on the rationale that in a high-quality signal, the mean HR or PR calculated by way of the BBIs should be consistent with that calculated as the number of detected BPM, as

$$Q_e = \frac{\frac{N}{t_e}}{\frac{1}{N-1} \sum_{i=1}^{N-1} \frac{60}{I(i)}}$$

where N is the number of detected beats in an epoch, t_e is the length of the epoch in minutes, and I is the BBI calculated from each successive pair of detected beats in seconds. Signal epochs with quality below a threshold value (e.g., $Q_e < 0.5$) are excluded from further processing.

Auto-detection of absent and continuous BP epochs

Absence detection and continuous BP period detection are performed in 30-s epochs. For absence detection, we implemented a threshold on the spectral power stored in the 99% occupied bandwidth of the band-pass filtered sensor output from CH1. Specifically, the threshold is chosen to be -45 dB, below which the epoch is labeled as absent. The auto-detection of continuous BP epochs is

based on the fact that if the heart and pulse signals are simultaneously present in an epoch, then the HR and PR calculated from the respective signals should be equal. We first used the absence detection method described above to identify whether signals are present in both channels. The mean HR and PR are then calculated for the identified epochs, and their absolute difference is taken as a similarity metric. An epoch is identified as a candidate for continuous BP detection if the absolute difference is less than 2 BPM. Last, continuous BP epochs are selected as candidate epochs with quality metric $Q_e > 0.5$ for both heart and pulse signals (fig. S20).

Evaluation in simulation aircraft cabin

We attached our metamaterial textile sensor prototype onto a seat in an aircraft cabin simulator, and a healthy male volunteer was seated as shown in Fig. 4D. Reference HR was recorded by an Apple Watch (version 7, Apple Inc.) worn on the left wrist. The evaluation trial lasted for a total of 50 min, comprising three consecutive periods. In the first and third 20-min periods, the volunteer was instructed to sit still in the upright position. In the middle 10-min period, the volunteer was instructed to get up from the seat to perform static running exercises. Sensor signals were recorded continuously for the entire duration. Continuous HR from our sensor was extracted following the methods outlined previously. Reference HR from the Apple Watch was obtained from the iOS Health application on a paired iPhone (version 13 Pro, Apple Inc.), which is provided as a minimum-maximum range every 2 min.

All experiments complied with a protocol approved by the National University of Singapore Institutional Review Board (NUS-IRB-2022-561). All subjects were volunteers, were informed of risks and benefits, and provided informed consent.

Supplementary Materials

This PDF file includes:

Figs. S1 to S23
Tables S1 to S5
Legends for movies S1 to S3
References (53–58)

Other Supplementary Material for this manuscript includes the following:

Movies S1 to S3

REFERENCES AND NOTES

1. D. J. Cook, J. C. Augusto, V. R. Jakkula, Ambient intelligence: Technologies, applications, and opportunities. *Pervasive Mob. Comput.* **5**, 277–298 (2009).
2. A. Haque, A. Milstein, L. Fei-Fei, Illuminating the dark spaces of healthcare with ambient intelligence. *Nature* **585**, 193–202 (2020).
3. G. Acampora, D. J. Cook, P. Rashidi, A. V. Vasilakos, A survey on ambient intelligence in healthcare. *Proc. IEEE* **101**, 2470–2494 (2013).
4. J. M. Fernandes, J. S. Silva, A. Rodrigues, F. Boavida, A survey of approaches to unobtrusive sensing of humans. *ACM Comput. Surv.* **55**, 1–28 (2023).
5. J. C. Kvedar, A. L. Fogel, E. Elenko, D. Zohar, Digital medicine's march on chronic disease. *Nat. Biotechnol.* **34**, 239–246 (2016).
6. M. Mercuri, I. R. Lorato, Y.-H. Liu, F. Wieringa, C. V. Hoof, T. Torfs, Vital-sign monitoring and spatial tracking of multiple people using a contactless radar-based sensor. *Nat. Electron.* **2**, 252–262 (2019).
7. M. Zhao, K. Hoti, H. Wang, A. Raghu, D. Katabi, Assessment of medication self-administration using artificial intelligence. *Nat. Med.* **27**, 727–735 (2021).
8. C. Massaroni, D. S. Lopes, D. Lo Presti, E. Schena, S. Silvestri, Contactless monitoring of breathing patterns and respiratory rate at the pit of the neck: A single camera approach. *J. Sens.* **2018**, 1–13 (2018).
9. B. P. Yan, W. H. S. Lai, C. K. Y. Chan, A. C. K. Au, B. Freedman, Y. C. Poh, M.-Z. Poh, High-throughput, contact-free detection of atrial fibrillation from video with deep learning. *JAMA Cardiol.* **5**, 105–107 (2020).
10. Z. Luo, J.-T. Hsieh, N. Balachandrar, S. Yeung, G. Pusioli, J. Luxenberg, G. Li, L.-J. Li, N. L. Downing, A. Milstein, L. Fei-Fei, Computer vision-based descriptive analytics of seniors' daily activities for

- long-term health monitoring, in *Proceedings of Machine Learning for Healthcare Conference* (2018), pp. 1–18.
11. M. Hu, G. Zhai, D. Li, Y. Fan, H. Duan, W. Zhu, X. Yang, Combination of near-infrared and thermal imaging techniques for the remote and simultaneous measurements of breathing and heart rates under sleep situation. *PLOS ONE* **13**, e0190466 (2018).
 12. Y. Ren, C. Wang, Y. Chen, J. Yang, H. Li, Noninvasive fine-grained sleep monitoring leveraging smartphones. *IEEE Internet Things J.* **6**, 8248–8261 (2019).
 13. J. Chan, T. Rea, S. Gollakota, J. E. Sunshine, Contactless cardiac arrest detection using smart devices. *NPJ Digit. Med.* **2**, 1–8 (2019).
 14. C. Li, V. M. Lubecke, O. Boric-Lubecke, J. Lin, A review on recent advances in Doppler radar sensors for noncontact healthcare monitoring. *IEEE Trans. Microw. Theor. Techniq.* **61**, 2046–2060 (2013).
 15. G. Wang, J.-M. Muñoz-Ferreras, C. Gu, C. Li, R. Gómez-García, Application of linear-frequency-modulated continuous-wave (LFMCW) radars for tracking of vital signs. *IEEE Trans. Microw. Theor. Techniq.* **62**, 1387–1399 (2014).
 16. X. Hui, E. C. Kan, Monitoring vital signs over multiplexed radio by near-field coherent sensing. *Nat. Electron.* **1**, 74–78 (2018).
 17. X. Hui, E. C. Kan, No-touch measurements of vital signs in small conscious animals. *Sci. Adv.* **5**, 1–8 (2019).
 18. J. Lee, A. J. Park, Y. Tanabe, A. S. Y. Poon, S. Kim, A microwave method to remotely assess the abdominal fat thickness. *AIP Adv.* **11**, 035111 (2021).
 19. Z. Zhuang, F. Wang, X. Yang, L. Zhang, C.-H. Fu, J. Xu, C. Li, H. Hong, Accurate contactless sleep apnea detection framework with signal processing and machine learning methods. *Methods* **205**, 167–178 (2022).
 20. Y. Liu, G. Zhang, C. G. Tarolli, R. Hristov, S. Jensen-Roberts, E. M. Waddell, T. L. Myers, M. E. Pawlik, J. M. Soto, R. M. Wilson, Y. Yang, T. Nordahl, K. J. Lizarraga, J. L. Adams, R. B. Schneider, K. Kiebert, T. Ellis, E. R. Dorsey, D. Katabi, Monitoring gait at home with radio waves in Parkinson's disease: A marker of severity, progression, and medication response. *Sci. Transl. Med.* **14**, ead9669 (2022).
 21. G. Chen, X. Xiao, X. Zhao, T. Tat, M. Bick, J. Chen, Electronic textiles for wearable point-of-care systems. *Chem. Rev.* **122**, 3259–3291 (2022).
 22. I. I. Shuvo, A. Shah, C. Dagdeviren, Electronic textile sensors for decoding vital body signals: State-of-the-art review on characterizations and recommendations. *Adv. Intell. Syst.* **4**, 2100223 (2022).
 23. L. Eskandarian, E. Lam, C. Rupnow, M. A. Meghraz, H. E. Naguib, Robust and multifunctional conductive yarns for biomedical textile computing. *ACS Appl. Electron. Mater.* **2**, 1554–1566 (2020).
 24. A. Alemayeen, S. Noghianian, On-body low-profile textile antenna with artificial magnetic conductor. *IEEE Trans. Antennas Propag.* **67**, 3649–3656 (2019).
 25. Q. H. Dang, S. J. Chen, D. C. Ranasinghe, C. Fumeaux, A frequency-reconfigurable wearable textile antenna with one-octave tuning range. *IEEE Trans. Antennas Propag.* **69**, 8080–8089 (2021).
 26. X. Tian, P. M. Lee, Y. J. Tan, T. L. Y. Wu, H. Yao, M. Zhang, Z. Li, K. A. Ng, B. C. K. Tee, J. S. Ho, Wireless body sensor networks based on metamaterial textiles. *Nat. Electron.* **2**, 243–251 (2019).
 27. X. Tian, Q. Zeng, D. Nikolayev, J. S. Ho, Conformal propagation and near-omnidirectional radiation with surface plasmonic clothing. *IEEE Trans. Antennas Propag.* **68**, 7309–7319 (2020).
 28. R. G. Perron, G. C. Huang, M. F. Iskander, Textile electromagnetic coupler for monitoring vital signs and changes in lung water content. *IEEE Antennas Wirel. Propag. Lett.* **14**, 151–154 (2015).
 29. P. Vélez, F. Martín, R. Fernández-García, I. Gil, Embroidered textile frequency-splitting sensor based on stepped-impedance resonators. *IEEE Sens. J.* **22**, 8596–8603 (2022).
 30. F. J. García-Vidal, A. I. Fernández-Domínguez, L. Martín-Moreno, H. C. Zhang, W. Tang, R. Peng, T. J. Cui, Spoof surface plasmon photonics. *Rev. Mod. Phys.* **94**, 025004 (2022).
 31. X. Tian, Q. Zeng, S. A. Kurt, R. R. Li, D. T. Nguyen, Z. Xiong, Z. Li, X. Yang, X. Xiao, C. Wu, B. C. K. Tee, D. Nikolayev, C. J. Charles, J. S. Ho, Implant-to-implant wireless networking with metamaterial textiles. *Nat. Commun.* **14**, 4335 (2023).
 32. X. Shen, T. J. Cui, D. Martín-Cano, F. J. García-Vidal, Conformal surface plasmons propagating on ultrathin and flexible films. *Proc. Natl. Acad. Sci. U.S.A.* **110**, 40–45 (2013).
 33. Z. Zhang, P. Sharma, J. Zhou, X. Hui, E. C. Kan, Furniture-integrated respiration sensors by notched transmission lines. *IEEE Sens. J.* **21**, 5303–5311 (2021).
 34. J. M. Bland, D. G. Altman, Statistical methods for assessing agreement between two methods of clinical measurement. *Lancet* **327**, 307–310 (1986).
 35. R. Wang, G. Blackburn, M. Desai, D. Phelan, L. Gillinov, P. Houghtaling, M. Gillinov, Accuracy of wrist-worn heart rate monitors. *JAMA Cardiol.* **2**, 104–106 (2017).
 36. S. R. Pasadyn, M. Soudan, M. Gillinov, P. Houghtaling, D. Phelan, N. Gillinov, B. Bittel, M. Y. Desai, Accuracy of commercially available heart rate monitors in athletes: A prospective study. *Cardiovasc. Diagn. Ther.* **9**, 379–385 (2019).
 37. R. Mukkamala, J. O. Hahn, O. T. Inan, L. K. Mestha, C. S. Kim, H. Toreyin, S. Kyal, Toward ubiquitous blood pressure monitoring via pulse transit time: Theory and practice. *IEEE Trans. Biomed. Eng.* **62**, 1879–1901 (2015).
 38. H. Gesche, D. Grosskurth, G. Küchler, A. Patzak, Continuous blood pressure measurement by using the pulse transit time: Comparison to a cuff-based method. *Eur. J. Appl. Physiol.* **112**, 309–315 (2012).
 39. R. C. Block, M. Yavarimanes, K. Natarajan, A. Carek, A. Mousavi, A. Chandrasekhar, C.-S. Kim, J. Zhu, G. Schifitto, L. K. Mestha, O. T. Inan, J.-O. Hahn, R. Mukkamala, Conventional pulse transit times as markers of blood pressure changes in humans. *Sci. Rep.* **10**, 16373 (2020).
 40. G. C. Ryde, H. E. Brown, N. D. Gilson, W. J. Brown, Are we chained to our desks? Describing desk-based sitting using a novel measure of occupational sitting. *J. Phys. Activ. Health* **11**, 1318–1323 (2014).
 41. P. C. Dempsey, N. Owen, S. J. H. Biddle, D. W. Dunstan, Managing sedentary behavior to reduce the risk of diabetes and cardiovascular disease. *Curr. Diab. Rep.* **14**, 522 (2014).
 42. J. Y. Chau, A. C. Grunseit, T. Chey, E. Stamatakis, W. J. Brown, C. E. Matthews, A. E. Bauman, H. P. van der Ploeg, Daily sitting time and all-cause mortality: A meta-analysis. *PLOS ONE* **8**, e80000 (2013).
 43. J. A. Caldwell, Fatigue in aviation. *Travel Med. Infect. Dis.* **3**, 85–96 (2005).
 44. C. Li, Z. Peng, T.-Y. Huang, T. Fan, F.-K. Wang, T.-S. Horng, J.-M. Munoz-Ferreras, R. Gomez-Garcia, L. Ran, J. Lin, A review on recent progress of portable short-range noncontact microwave radar systems. *IEEE Trans. Microw. Theor. Techn.* **65**, 1692–1706 (2017).
 45. M. Roudjane, S. Bellemare-Rousseau, E. Drouin, B. Belanger-Huot, M.-A. Dugas, A. Miled, Y. Messaddeq, Smart T-shirt based on wireless communication spiral fiber sensor array for real-time breath monitoring: Validation of the technology. *IEEE Sens. J.* **20**, 10841–10850 (2020).
 46. D. Wu, D. Zhang, C. Xu, H. Wang, X. Li, Device-free WiFi human sensing: From pattern-based to model-based approaches. *IEEE Commun. Mag.* **55**, 91–97 (2017).
 47. S. Dhupkariya, V. K. Singh, A. Shukla, A review of textile materials for wearable antenna. *J. Microw. Eng. Technol.* **1**, (2014).
 48. IEEE standard for safety levels with respect to human exposure to electric, magnetic, and electromagnetic fields, 0 Hz to 300 GHz, in *IEEE Std C95.1-2019* (Revision of IEEE Std C95.1-2005/ Incorporates IEEE Std C95.1-2019/Cor 1-2019, 2019), pp. 1–312.
 49. W. Lu, M. M. Nystrom, P. J. Parikh, D. R. Fooshee, J. P. Hubenschmidt, J. D. Bradley, D. A. Low, A semi-automatic method for peak and valley detection in free-breathing respiratory waveforms. *Med. Phys.* **33**, 3634–3636 (2006).
 50. J. Pan, W. J. Tompkins, A real-time QRS detection algorithm. *IEEE Trans. Biomed. Eng.* **BME-32**, 230–236 (1985).
 51. H. Sedghamiz, Matlab implementation of Pan Tompkins ECG QRS detector (2014); https://researchgate.net/publication/313673153_Matlab_Implementation_of_Pan_Tompkins_ECG_QRS_detector.
 52. C. Lays, C. Ley, O. Klein, P. Bernard, L. Licata, Detecting outliers: Do not use standard deviation around the mean, use absolute deviation around the median. *J. Exp. Soc. Psychol.* **49**, 764–766 (2013).
 53. D. Teichmann, J. Foussier, J. Jia, S. Leonhardt, M. Walter, Noncontact monitoring of cardiorespiratory activity by electromagnetic coupling. *IEEE Trans. Biomed. Eng.* **60**, 2142–2152 (2013).
 54. Y. Lee, J. Y. Park, Y. W. Choi, H. K. Park, S. H. Cho, S. H. Cho, Y. H. Lim, A novel non-contact heart rate monitor using impulse-radio ultra-wideband (IR-UWB) radar technology. *Sci. Rep.* **8**, 1–10 (2018).
 55. X. Hui, E. C. Kan, Seat integration of RF vital-sign monitoring, in *2019 IEEE MTT-S International Microwave Biomedical Conference (IMBioC)* (IEEE, 2019).
 56. L. Wen, Y. Gao, C. Gu, J. Mao, PhysioChair: A dual-frequency radar system for noninvasive and continuous detection of physiological signatures. *IEEE Sens. J.* **22**, 8224–8233 (2022).
 57. A. Wang, D. Nguyen, A. R. Sridhar, S. Gollakota, Using smart speakers to contactlessly monitor heart rhythms. *Commun. Biol.* **4**, 1–12 (2021).
 58. D. Andreuccetti, R. Fossi, C. Petrucci, An Internet resource for the calculation of the dielectric properties of body tissues in the frequency range 10 Hz - 100 GHz, IFAC-CNR, Florence (Italy) (1997).

Acknowledgments

Funding: This work by the authors is partially supported by grants from Advanced Research and Technology Innovation Centre (ARTIC), National University of Singapore grant A-0005947-11-00 (Y.L. and J.S.H.) and RIE2020 Industry Alignment Fund—Industry Collaboration Projects (IAF-ICP), National Research Foundation and A*STAR, Singapore grant I2001E0059—SIA-NUS Digital Aviation Corp Lab (P.C., C.W., and J.S.H.). **Author contributions:** Conceptualization: D.T.N., X.T., and J.S.H. Methodology: D.T.N., Q.Z., X.T., and J.S.H. Investigation: D.T.N., Q.Z., and X.T. Visualization: D.T.N., Q.Z., and X.T. Supervision: J.S.H. Funding acquisition: P.C., C.W., Y.L., and J.S.H. Writing—original draft: D.T.N. and Q.Z. Writing—review and editing: D.T.N., Q.Z., X.T., P.C., C.W., Y.L., and J.S.H. **Competing interests:** D.T.N., Q.Z., X.T., and J.S.H. are inventors on a pending patent related to this work filed by Intellectual Property Office of Singapore (IPOS), 10202204979V, on 12 May 2022. The authors declare no other competing interests. **Data and materials availability:** All data needed to evaluate the conclusions in the paper are present in the paper and/or the Supplementary Materials.

Submitted 16 July 2023

Accepted 1 December 2023

Published 5 January 2024

10.1126/sciadv.adj6613

Ambient health sensing on passive surfaces using metamaterials

Dat T. Nguyen, Qihang Zeng, Xi Tian, Patrick Chia, Changsheng Wu, Yuxin Liu, and John S. Ho

Sci. Adv. **10** (1), eadj6613. DOI: 10.1126/sciadv.adj6613

View the article online

<https://www.science.org/doi/10.1126/sciadv.adj6613>

Permissions

<https://www.science.org/help/reprints-and-permissions>

Use of this article is subject to the [Terms of service](#)

Science Advances (ISSN 2375-2548) is published by the American Association for the Advancement of Science. 1200 New York Avenue NW, Washington, DC 20005. The title *Science Advances* is a registered trademark of AAAS.

Copyright © 2024 The Authors, some rights reserved; exclusive licensee American Association for the Advancement of Science. No claim to original U.S. Government Works. Distributed under a Creative Commons Attribution NonCommercial License 4.0 (CC BY-NC).